nature communications

Article

https://doi.org/10.1038/s41467-026-72751-8

Observation of Restored Adiabatic State Transfer in Time-Modulated Non-Hermitian Systems

Received: 11 November 2025

Accepted: 23 April 2026

Published online: 12 May 2026

Check for updates

Xiaowei Wang[1,5], Ievgen I. Arkhipov[2,5], Quan Lin[3], Huixia Gao[3], Dengke Qu[3], Lei Xiao[3], Franco Nori[4] & Peng Xue[3]

Exceptional points (EPs) have attracted extensive research interest due to their intriguing properties. One of the hallmarks of EP physics is that dynamically encircling the EPs induces chiral mode switching, arising from the breakdown of adiabaticity due to the presence of a complex spectrum in the system's Hamiltonian. While such chiral mode behavior has been widely observed experimentally, achieving truly adiabatic, and thus symmetric, state transfer, regardless of the winding direction, in time-modulated non-Hermitian systems has remained elusive. In this work, we demonstrate that this long-sought adiabatic state dynamics can indeed be restored. By steering a two-mode photonic setup along specifically designed trajectories in parameter space, we realize conditions where the associated non-Hermitian evolution operator acquires a purely real spectrum. Moreover, our experimental platform enables controlled switching between symmetric (adiabatic) and chiral (non-adiabatic) state-transfer regimes for the same set of initial modes, thus effectively implementing a universal symmetric-asymmetric two-mode switch. Our results therefore open new avenues for harnessing unique topological spectral properties of non-Hermitian systems, paving the way for the practical design of versatile optical wave-manipulation devices and for advancing both classical and quantum information technologies.

Non-Hermitian systems with gain and loss exhibit rich physical phenomena that are fundamentally distinct from Hermitian quantum systems, attracting broad interest in current research[1]. Their inherently complex energy spectra give rise to unique spectral degeneracies known as EPs[2–4], which are characterized by the simultaneous coalescence of both eigenvalues and their corresponding eigenvectors. The topological structure near EPs underlies a variety of counterintuitive phenomena[5–16], ranging from nonreciprocal optoelectronic devices[5–7] and unconventional lasing effects[9–11] to enhanced sensing[12–14], to name a few (see also reviews[17,18]).

Exceptional points endow non-Hermitian spectra with a characteristic topological structure that can profoundly affect their state evolution. In particular, when system parameters trace a closed loop around an EP, the associated Riemann-sheet topology can induce a symmetric permutation of eigenstates, such that an eigenmode does not return to itself after a single cycle and the final state depends solely on the initial condition, irrespective of the winding direction. This symmetric state-exchange effect has been predicted theoretically[19,20] and observed experimentally[21–26] using quasi-static, namely stroboscopic, protocols, where eigenstates are independently probed at

[1]Beijing Computational Science Research Center, Beijing, China. [2]Joint Laboratory of Optics of Palacký University and Institute of Physics of CAS, Faculty of Science, Palacký University, Olomouc, Czech Republic. [3]School of Physics, Southeast University, Nanjing, China. [4]Quantum Information Physics Theory Research Team, Quantum Computing Center, RIKEN, Wakoshi, Saitama, Japan. [5]These authors contributed equally: Xiaowei Wang, Ievgen I. Arkhipov
e-mail: gnep.eux@gmail.com

successive points in parameter space without invoking continuous time evolution.

When the same EP-encircling is implemented dynamically, however, qualitatively different behavior emerges. A prominent consequence is chiral mode transfer: when dynamically encircling an EP, the final state depends solely on the encircling direction regardless of the initial state[27–37]. The complex Riemann surface structure in the system's spectrum underlies this chiral behavior, namely, the eigenstate with the larger imaginary part of the eigenvalue is preferentially populated due to non-adiabatic transitions (NATs) which occur during the state evolution[27]. While this chiral mode behavior has been extensively studied both theoretically[38–40] and experimentally[27–32,35,36,41], achieving truly adiabatic and symmetric state transfer in time-modulated non-Hermitian systems has remained a formidable challenge.

Adiabatic and symmetric state transfer can be restored in non-Hermitian systems, as demonstrated by the theoretical study[42]. In this context, the restored adiabaticity refers to the absence of discontinuous NATs during the state evolution. Such behavior is realized by dynamically encircling an EP along suitably designed trajectories in parameter space, for which the non-Hermitian evolution operator exhibits a purely real spectrum. The resulting suppression of NATs thus enables smooth and symmetric state transfer. This behavior is in sharp contrast to previously studied dynamical EP-encircling protocols, where complex spectra generically trigger non-adiabatic jumps and give rise to chiral, direction-dependent state transfer[27,28].

Here, we report the experimental observation of adiabatic and symmetric state transfer in a time-modulated non-Hermitian photonic platform. By monitoring the polarization state of a laser pulse under controlled intensity, phase, and polarization modulations, we realize specific closed loops in the parameter space that dynamically encircle an EP. Along these specially chosen trajectories, we demonstrate the full restoration of adiabaticity, independent of the direction of encirclement.

Crucially, the same platform also enables us to switch between symmetric (adiabatic) and chiral (non-adiabatic) state-transfer regimes for a fixed initial set of eigenstates. This constitutes the effective realization of a programmable symmetric-chiral state switch, a capability that was previously considered unattainable in non-Hermitian two-level systems. Specifically, for a given initial and final Hamiltonian, the nature of the state transfer (symmetric or asymmetric) can be selected solely through the proper choice of parameter modulation within a single physical platform. This work provides an alternative route for the dynamical control of states in non-Hermitian systems, providing opportunities for next-generation optical wave-manipulation devices and advancing both classical and quantum technologies.

Results

Adiabatic and symmetric state transfer in time-modulated non-Hermitian systems

In a properly chosen orthonormal basis denoted by $\{|0\rangle, |1\rangle\}$, we consider a two-level non-Hermitian Hamiltonian (NHH)[42]

$$H_0 = \begin{pmatrix} -i\upsilon + \epsilon & u + i\kappa \\ u + i\kappa & i\upsilon - \epsilon \end{pmatrix}, \tag{1}$$

where all parameters in Eq. (1) are assumed to be real, and the non-Hermiticity is introduced by the parameters υ and κ[43]. Accordingly, the NHH governs the state evolution via the Schrödinger equation (in units $\hbar = 1$) $i\partial_t|\psi(t)\rangle = H_0|\psi(t)\rangle$.

The spectrum of the NHH reads

$$E_{\pm} = \pm\sqrt{(u - \upsilon + i\kappa - i\epsilon)(u + \upsilon + i\kappa + i\epsilon)} \in \mathbb{C}, \tag{2}$$

which exhibits EPs when $\{\upsilon_{\rm EP} = \pm u, \epsilon_{\rm EP} = \pm\kappa\}$[42]. When $\kappa = 0$, the NHH in Eq. (1) reduces to the standard NHH known to exhibit chiral state transfer while dynamically encircling the EP[27]. This chiral behavior originates from the complex spectrum of the NHH: as the eigenstates evolve, the system undergoes NATs that drive it toward the least-loss state with the maximal imaginary part of the eigenvalue. Consequently, the system preferentially evolves into this least-loss state, thus resulting in the observed chirality[17]. This mechanism further suggests that if an NHH could be engineered to host EPs while maintaining a purely real spectrum, NATs would be suppressed, thus enabling the long-sought realization of adiabatic and symmetric state transfer that exploits the unique EP topology.

A theoretical study[42] has shown that such adiabatic and therefore symmetric state transfer, in two-level NHH systems, can indeed be restored when the system parameters are constrained to a hyperboloid submanifold of the parameter space. An extension of this protocol to multi-level systems is also discussed in Ref. 44. In particular, by employing the parametrization:

$$\begin{aligned} \upsilon &= \alpha\sinh\phi_i\sin\phi_r, & \epsilon &= \alpha\cosh\phi_i\cos\phi_r, \\ u &= \alpha\cosh\phi_i\sin\phi_r, & \kappa &= \alpha\sinh\phi_i\cos\phi_r, \end{aligned} \tag{3}$$

with $\phi = \phi_r + i\phi_i = \arctan(x + iy)^{-1} \in \mathbb{C}$ and $\alpha = x\sinh\phi_i/\sin\phi_r \in \mathbb{R}$, one transforms the original NHH with complex spectrum into NHH

$$H_0 \to H = \alpha\begin{pmatrix} \cos\phi & \sin\phi \\ \sin\phi & -\cos\phi \end{pmatrix}, \tag{4}$$

which is characterized exclusively by real eigenvalues

$$E_{1,2} = \mp\alpha, \tag{5}$$

in the entire (x, y) plane, and where we arrange the eigenvalues in descending order, namely $E_1 \geq E_2$. The explicit form of the eigenvectors of the NHH H is given in "Methods".

Specifically, the system parameters in Eq. (3) define a two-dimensional (2D) hyperboloid embedded in the 4D parameter space $(\epsilon, u, \upsilon, \kappa)$ satisfying $\epsilon^2 + u^2 - \upsilon^2 - \kappa^2 = \alpha^2$ (see also Supplementary Information for an intuitive geometric visualization of this manifold). Importantly, by restricting the system parameters to such a 2D manifold within the full 4D parameter space, one can effectively reduce the NHH H_0 in Eq. (1), which generally exhibits complex eigenvalues, into a parameter regime where the spectrum becomes purely real. Physically, this restriction enforces a balance between gain and loss that removes the imaginary part of the spectrum.

Owing to the hyperbolic embedding defined by Eq. (3), each point (x, y) uniquely determines a single point in $(\epsilon, u, \upsilon, \kappa)$ in the full parameter space, and hence a unique Hamiltonian. Therefore, the spectrum of the NHH H is well defined. More precisely, the representation of this hyperbolic mapping via Eq. (4) is one-to-one and continuous throughout the parameter space except at an EP, where the parametrization becomes singular due to the defectiveness of the Hamiltonian H_0. This singularity, however, reflects a breakdown of the coordinate representation rather than of the Hamiltonian itself, which remains well-defined in the original parametrization (see below).

The corresponding EPs, in the spectrum of the NHH H, appear as branch points of two intersected real-valued Riemann sheets located at $(x = 0, y = \pm 1)$. Notably, the eigenvalues of the NHH H remain well-defined at the EP ($\alpha_{EP} = 0$), while the eigenvectors given in Eqs. (11) and (12) become singular ($\phi_{EP} \to -i\infty$). This behavior is a direct manifestation of eigenvector coalescence in the original representation of the NHH H_0 in Eq. (1) (see Supplementary Information for details). We emphasize that, in our protocol, the EP is only encircled and never crossed. Consequently, the eigenvectors of H and their evolution along the winding trajectories remain well-defined throughout the process.

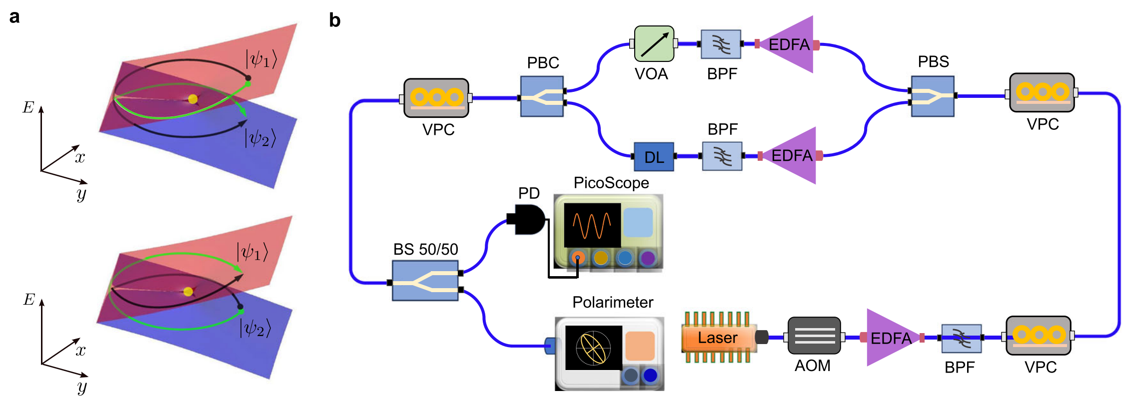

Fig. 1 | Schematic illustration of the experimental implementation. **a** Schematic diagram of adiabatic evolution by dynamically encircling the EP in a two-level non-Hermitian system. We present schematic trajectories with different encircling directions starting from the two involved Riemann sheets, where the red and blue surfaces represent the two eigenenergies. The yellow sphere represents the EP point. The state transfer is observed to be independent of the direction of the encirclement, where the green/black trajectories denote clockwise/counterclockwise encirclement. **b** Experimental setup. The seed pulse module consists of a distributed feedback laser and an acousto-optic modulator (AOM) for generating pulses, an erbium-doped fiber amplifier (EDFA) with integrated variable attenuator for pulse amplification, a narrow bandpass filter (BPF) to suppress the excessive noise introduced by the EDFA, and a variable polarization controller (VPC) for preparing the initial polarization state. Two VPCs are then used to couple the polarization components to implement unitary operations. These non-unitary operations are realized by using the polarized beam splitter (PBS), EDFAs, the optical delay line (DL), a variable optical attenuator (VOA), and the polarized beam combiner (PBC), where the horizontal and vertical polarization components can be independently controlled along two separate optical paths. Finally, half of the pulses are routed to a monitoring module equipped with an InGaAs photodetector (PD) and a PicoScope, and the remaining pulses are used for polarization state analysis via a polarimeter.

Interestingly, the branch cut ($x = 0, -1 < y < 1$) coincides with a diabolic line defined by the condition $E_{1,2} = 0$ in Eq. (5). As a result, the EP-encircling protocol with restored adiabaticity considered here, illustrated in Fig. 1a and discussed in detail below, necessarily involves traversing this diabolic degeneracy. This observation motivates a clarification of the notion of adiabaticity used in the present protocol. In particular, adiabaticity in the Berry–Kato sense, which is based on the following instantaneous eigenstate in the presence of a finite spectral gap, is not directly applicable here. The term "adiabatic" we use is in the operational sense of the absence of discontinuous non-adiabatic transitions. This situation differs from conventional EP-encircling schemes in systems with complex spectra, where branch cuts do not generally coincide with extended real-energy degeneracies and the assumptions underlying the standard adiabatic theorem may still be fulfilled. Here, "adiabatic" therefore refers exclusively to a dynamical regime in which sufficiently slow parameter modulation yields continuous state evolution, with adiabaticity identified operationally through the absence of NATs. This dynamical behavior is enabled by the absence of an imaginary component in the spectrum of the NHH H along the encircling trajectory, which suppresses mode-selective amplification and thereby prevents discontinuous NATs[27]. In what follows, unless explicitly stated otherwise, we use the term adiabaticity exclusively in this operational sense.

In this respect, the symmetric state-switching protocol based on dynamical EP encirclement in such systems with a purely real spectrum echoes the adiabatic rapid passage (ARP) protocol familiar from Hermitian systems, where robust state transfer can be similarly achieved through slow parameter variation by traversing diabolical degeneracies during the state evolution[45]. Similar parallels between these Hermitian and non-Hermitian state-flipping protocols have already been discussed and experimentally explored in ref. 33. Crucially, however, compared to ref. 33, the protocol experimentally implemented here operates in a parameter regime where the diabolic line emerges as the branch cut terminating at EPs, and where the continuous state evolution remains entirely free of NATs.

Experimental simulation of adiabatic and symmetric state transfer

We now demonstrate that the dynamics governed by the Hamiltonian in Eq. (4) are independent of NATs, implying that the system can evolve adiabatically along an orbit in parameter space while dynamically encircling an EP. We first choose the time-evolution trajectory as

$$\begin{aligned} x(t) &= r\sin(\omega t + \phi_0), \\ y(t) &= 1 - r\cos(\omega t + \phi_0), \end{aligned} \tag{6}$$

where r, ω, ϕ_0 are real constants. Correspondingly, we change $H(t)$ in Eq. (4) along with $x(t)$ and $y(t)$. This path traces a circle with a radius r on the plane (x, y), centered at the EP, $(x, y)_{\rm EP} = (0, 1)$. The starting point corresponds to the phase $\phi_0 = \pi$, where the two energy levels $E_{1,2}$ are maximally separated. For angular frequencies $\omega > 0$ $(\omega < 0)$, the encircling direction is counterclockwise (clockwise). Note that a loop in the 2D plane (x, y) corresponds to a loop on a 4D hyperboloid in the system parameter space, according to the definition of parameterization (see also Supplementary Information).

In our experiment, we encode the qubit basis in the horizontal and vertical polarization states of a light pulse, namely, $|0\rangle \equiv |H\rangle$ and $|1\rangle \equiv |V\rangle$. The two orthogonal polarization components are coupled to each other via a polarization controller. Figure 1b shows the experimental optical setup used to simulate the adiabatic dynamics in a non-Hermitian system described by the NHH in Eq. (4). The experimental platform consists of three main stages: state preparation, evolution, and measurement (see also "Methods").

For a given initial polarization state $|\Psi_0\rangle$, the system evolution is described by

$$|\Psi(t)\rangle = U(t)|\Psi_0\rangle, \tag{7}$$

where $|\Psi(t)\rangle = [a(t), b(t)]^T$ represents the polarization state at evolution time t, with $a(t)$ and $b(t)$ denoting the horizontal and vertical field components, respectively.

In the experiment, we simulate the continuous system dynamics, generated by a time-dependent NHH $H(t)$, by constructing a family of "static" non-unitary evolution operators $U(t)$, each of which corresponds to the time evolution from $t = 0$ to a chosen target time t. Specifically, in the experiment, we select 21 representative target times that include the initial time. Each target time t_q corresponds to an independently constructed operator $U(t_q)$. For example, for $\omega t_q = \pi$, the operator $U(t_q)$ represents the evolution from $t = 0$ to $t_q = \pi/\omega$. This operator is then applied to the initial state in a single experimental run

https://doi.org/10.1038/s41467-026-72751-8

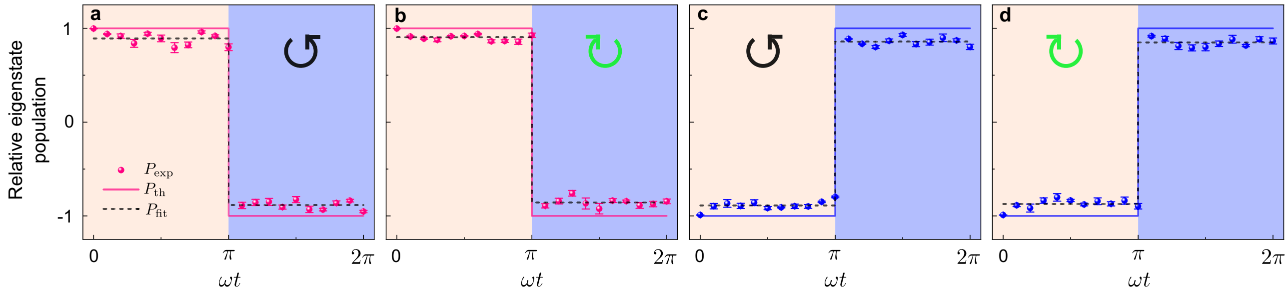

Fig. 2 | Experimental observation of adiabatic state transfer while dynamically encircling around an EP. The circle in the inset represents the counterclockwise or clockwise encircling direction in the (x, y)-plane defined in Eq. (6), as shown in Fig. 1**a**. **a**, **b** The initial state is chosen as $|\psi_1\rangle$ on the E_1 energy surface. **c**, **d** The initial state is chosen as $|\psi_2\rangle$ on the E_2 energy surface. The region from 0 to π along the horizontal axis represents uncompleted state switching for times $0 \le t \le T/2$ (shaded light red region), and the region from π to 2π along the horizontal axis, corresponding to times $T/2 \le t \le T$ (shaded light blue region), represents successful state switching. The solid circles represent the experimental data, and the solid lines denote the theoretical prediction. Dashed curves are obtained by numerically fitting the experimental data, where the fitting values obtained for the uncompleted/completed state switching region of each panel are: **a** 0.89/−0.88; **b** 0.90/−0.86; **c** −0.89/0.86; **d** −0.87/0.85. Error bars represent the standard deviation of the measurement results. The discrepancy between experiment and theory mainly stems from the uncertainty of the instantaneous eigenstates and unavoidable noise during the experiment. The other parameters are $r = 0.5$ and $\phi_0 = \pi$.

(as shown in Fig. 1). As such, hereafter, unless stated otherwise, the terms "time evolution", "dynamically encircling", and "system dynamics" refer experimentally to this simulated evolution, rather than to a genuine "in-situ" encircling.

To obtain each $U(t_q)$, we first numerically integrate the Schrödinger equation from $t = 0$ to $t = t_q$. This integration is performed using $N = 5 \times 10^4$ time steps, which ensures the convergence of the time-ordered exponential (see also Supplementary Information). Formally, the evolution operator is approximated as

$$U(t_q) \approx \prod_{n=1}^{N} \exp[-iH(t_n)\,\delta t], \tag{8}$$

where $\delta t = t_q/N$ and $t_n = (n - \frac{1}{2})\delta t$ denotes the midpoint of each integration interval. Each such numerically constructed operator $U(t_q)$ is then physically implemented by appropriately configuring the optical elements, thereby directly mapping the integrated evolution onto the output state. Repeating this procedure for different target times t_q allows us to efficiently simulate the continuous dynamics of the system without relying on incremental or stroboscopic parameter modulation.

In the experiment, we implement this sequence of operators using variable polarization controllers and a split-path gain-loss module within a two-mode optical platform (see also "Methods"). The non-unitary operator $U(t)$ is experimentally implemented on the basis of the singular value decomposition $U(t) = R_1 L R_2$, where t represents the time parameter, which refers to a specific moment corresponding to the point on the trajectory of the parameters that we select in our experiment. The operators R_1 and R_2 are unitary matrices which can be readily realized using a set of wave plates with two quarter-wave plates and one half-wave plate at rotatable angles[46]. The operator L is a real positive semi-definite diagonal matrix in the following form $L = \mathrm{diag}[l_1, l_2]$. The experimental parameters varied for each data point are the rotation angles in the two variable polarization controllers to implement two unitary operators, and the gain/loss ratios related to the attenuation of the variable optical attenuator and the gain of the erbium-doped fiber amplifier. These are derived explicitly from the singular value decomposition of $U(t)$, which is calculated using the parameters of the system's Hamiltonian. This allows us to reconstruct the state trajectory with high fidelity, avoiding the cumulative noise of long-loop light evolution associated with a continuous implementation.

We choose the initial state of the system as one of the right eigenstates of the NHH H, namely, $|\Psi_0\rangle = |\psi_k(t=0)\rangle$ $(k = 1, 2)$. To track the state dynamics, we measure the relative eigenstate population[47]

$$P(t) = \frac{|\langle\eta_1(t)|\Psi(t)\rangle|^2 - |\langle\eta_2(t)|\Psi(t)\rangle|^2}{\sum_{k=1,2}|\langle\eta_k(t)|\Psi(t)\rangle|^2}, \tag{9}$$

where $|\langle\eta_k(t)|\Psi(t)\rangle|^2$ is the fidelity between the evolving state $|\Psi(t)\rangle$ and the instantaneous left eigenstates $|\eta_k(t)\rangle$ of the NHH. The relative eigenstate population can take values within the interval $P \in [-1, 1]$. When P approaches 1, the evolving state almost entirely populates the first eigenstate $|\psi_1(t)\rangle$. Conversely, as P approaches −1, it converges to the second eigenstate $|\psi_2(t)\rangle$. Here, "instantaneous" means that the eigenvectors of the NHH are calculated independently at each time step, for the corresponding values of the parameters (x, y).

At the beginning, we select the initial state as $|\psi_1\rangle$ on the upper energy surface of Fig. 1a. As illustrated in Fig. 2a, in the experiment when the EP is encircled counterclockwise within the time $0 \le t \le T/2$, the relative eigenstate population $P_{\rm exp}(t)$ always approaches 1, indicating that the evolving state $|\Psi_{\rm exp}(t)\rangle$, governed by the NHH, is always close to in the first eigenstate $|\psi_1(t)\rangle$. Meanwhile, the state fidelity $|\langle\psi_1(t)|\Psi_{\rm exp}(t)\rangle|^2$ in this region exceeds 92.91%.

In contrast, during the second half of the cycle, when $T/2 \le t \le T$ in Fig. 2a, the relative eigenstate population $P_{\rm exp}(t)$ approaches −1, and the fidelity between $|\Psi_{\rm exp}(t)\rangle$ and $|\psi_2(t)\rangle$ is larger than 94.38%, indicating that the system state successfully switches from $|\psi_1\rangle$ to $|\psi_2\rangle$. These results imply that after completing the full cycle around the EP, the eigenstates undergo an exchange from $|\psi_1\rangle$ to $|\psi_2\rangle$. When reversing the encirclement direction to clockwise in Fig. 2b, the state dynamics exhibits a similar behavior: the initial eigenstate $|\psi_1\rangle$ is successfully switched to the eigenstate $|\psi_2\rangle$ at the end of the entire loop around the EP. This confirms that the state transfer is independent of the direction of the encirclement, thus demonstrating the adiabatic nature of the state evolution.

When we consider changing the initial state to $|\psi_2\rangle$ on the lower energy surface, a similar phenomenon is observed as demonstrated in Fig. 2c, d, where the initial eigenstate $|\psi_2\rangle$ is successfully switched to the eigenstate $|\psi_1\rangle$ at the end of the entire loop around the EP. This result also indicates the occurrence of adiabatic state transfer. We note that the apparent abrupt change of the projection of the evolving state on the instantaneous eigenstates at $t = T/2$ in Fig. 2, corresponding to the crossing of the diabolical line, arises from the interchange of the instantaneous eigenstates at this degeneracy, in accordance with the adopted labeling convention $E_1 \ge E_2$. Importantly, the state evolution remains fully continuous across this degeneracy, as further illustrated by complementary fidelity plots between the evolving and initial states provided in

https://doi.org/10.1038/s41467-026-72751-8

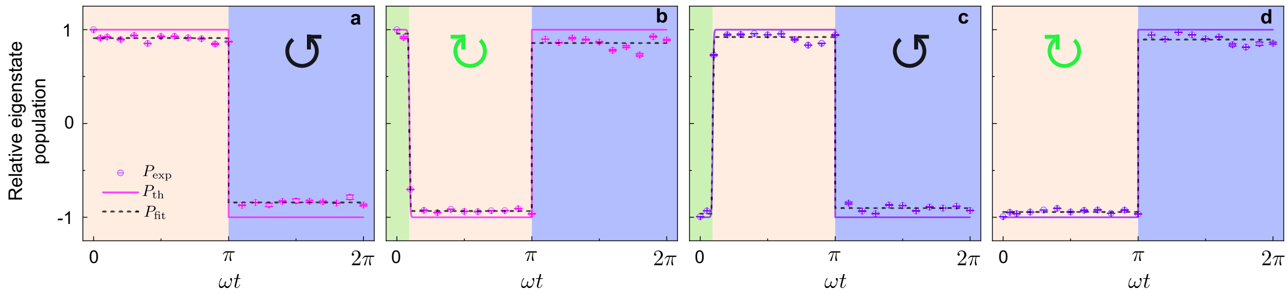

Fig. 3 | Experimental observation of chiral state transfer while dynamically encircling an EP. a, **b** The initial state is chosen as $|\psi_1'\rangle$. **c**, **d** The initial state is chosen as $|\psi_2'\rangle$. The circle in the inset represents the counterclockwise or clockwise encircling direction in the (x, y)-plane defined in Eq. (6), and the corresponding trajectory in the Riemann surface is shown in the Supplementary Information. The moment when the relative eigenstate population switches between +1 and −1 represents the occurrence of the state transfer. **b**, **c** The non-adiabatic jumps occur in the first interface near the starting point. The other descriptions are the same as those in Fig. 2.

the Supplementary Information. The observed continuous adiabatic behavior thus stands in stark contrast to previously studied non-Hermitian systems with EPs, where the presence of complex Riemann surfaces leads to non-adiabatic transitions during state evolution.

Importantly, the symmetric state-switching protocol demonstrated here is not restricted to specific winding periods T or particular EP-encircling trajectory shapes in the (x, y)-space[44]. Instead, it remains effective for a broad range of system parameters in Eq. (6), provided that the system evolution is sufficiently slow to suppress fast diabatic effects (see also Supplementary Information). This behavior differs from the scenario considered in ref. 33, where maintaining the adiabatic character of the EP-encircling protocol requires additional constraints on the system parameters.

We further emphasize that the observed adiabatic symmetric state transfer remains robust even when the NHH H in Eq. (4) is weakly perturbed so that its spectrum becomes complex, provided that the perturbations are sufficiently small to prevent the onset of NATs. Additional details and supporting analysis are provided in the Supplementary Information.

Experimental simulation of chiral state transfer

To confirm that the above parameter modulations indeed restore adiabaticity, we further present an experimental analysis of chiral state transfer realized in the same optical setup. For this purpose, we introduce another NHH H' that can directly induce the chiral state-switching behavior in the system's dynamics, namely

$$H' = C[(ix - y)\hat{\sigma}_z + i\hat{\sigma}_x], \tag{10}$$

where $C = \sqrt{y_0^2 - 1}\,\sin(\mathrm{arctanh}(y_0^{-1}))$ is a scaling factor with $y_0 = const$, and the system parameters (x, y) are time-modulated in the same manner as in Eq. (6). This particular choice of C ensures that at $t = 0$, when $(x = 0, y = y_0)$, the NHH H in Eq. (4) and the NHH H' in Eq. (10) coincide, namely, they possess identical eigenspectra at the initial time. Moreover, the real spectrum of H' is similar to that of H, including the EP at the same location $(x = 0, y = 1)$. Importantly, the spectrum of H', compared to H, exhibits the imaginary part, which plays the key role in inducing the NATs and therefore the chiral mode behavior occurs (see Supplementary Information for details). Thus, by implementing both NHHs, H and H', using the same experimental setup enables a controlled switching between adiabatic (symmetric) and non-adiabatic (chiral) mode-transfer regimes for the same set of eigenstates, as we demonstrate below.

We also implemented an experiment analogous to that described in the previous section on adiabatic state transfer. Here, we select the winding speed of $\omega = \pi/500$. As illustrated in Fig. 3, starting from different initial states $|\psi_k'\rangle$ (identical to $|\psi_k\rangle$ at $t = 0$), a complete counterclockwise encirclement of the EP drives the relative eigenstate population $P_{\rm exp}(t)$ toward −1, indicating that the final state always evolves into $|\psi_2'\rangle$, as shown in Fig. 3a, c. Conversely, clockwise encirclement always results in the final state $|\psi_1'\rangle$, we can see the final relative eigenstate population $P_{\rm exp}(t)$ always approaching 1 in Fig. 3b, d. This experimental observation thus confirms the established results on chiral mode switching in a two-level non-Hermitian system while dynamically encircling an EP[17]. This chirality arises because of NATs due to the nonzero difference in the imaginary parts of the two eigenenergies[27]. Contrary to the adiabatic dynamics, the observed asymmetry indicates that, in this case, the encircling direction rather than the initial conditions determines the final state.

Discussion

Although the protocol presented here has been implemented using a classical optical platform, its extension to the quantum regime, for instance, using single photons, is in principle feasible[36,37] and represents a promising direction toward the realization of robust quantum gates. In the classical setting with coherent light, optical losses can be compensated by amplifying elements, which may also provide controlled gain along the propagation path. In contrast, in the quantum regime, linear amplification unavoidably introduces quantum noise, which degrades coherence and fidelity of fragile quantum states[48]. To circumvent this limitation, relative gain can instead be implemented using purely passive attenuation, thereby avoiding noise injection[49]. This approach is inherently probabilistic, as not all photons survive the evolution, and consequently requires post-selection to discard loss events. While such a passive strategy increases overall losses and limits practical scalability, it nevertheless provides a viable route for experimentally accessing the quantum regime without compromising state coherence.

The non-Hermitian state transfer protocol implemented here can also be understood as a natural extension of the ARP protocol known in Hermitian systems[33,45]. An important conceptual distinction between the two is the role played by dissipation. In Hermitian settings, dissipation and decoherence are typically detrimental and must be minimized to preserve adiabatic state transfer. By contrast, in the non-Hermitian framework experimentally realized here, dissipation is not merely assumed but directly exploited as a control resource. Specifically, the engineered non-Hermitian dynamics give rise to parameter-space trajectories along which the spectrum of the effective Hamiltonian becomes purely real, thus suppressing mode-selective amplification and preventing discontinuous NATs during the EP encirclement. As a result, dissipation plays a constructive role in stabilizing the adiabatic dynamical state evolution and enabling symmetric, direction-independent state transfer. Our experimental findings thus further highlight how non-Hermitian control can transform dissipation from a limiting factor into a functional element for stable state manipulation in real-world dissipative photonic architectures.

https://doi.org/10.1038/s41467-026-72751-8

In this work, we report experimental evidence that adiabatic state evolution is fully restored during an EP-encircling protocol, which is realized through a sequence of individual evolution operators that scan the parameter space. This is achieved by selecting trajectories in parameter space along which the evolution operator attains a real spectrum. Using a two-mode optical platform, we realize adiabatic evolution by manipulating the polarization state of a laser pulse through precisely controlled intensity and phase modulation operations.

Furthermore, we experimentally demonstrate the ability to switch between symmetric (adiabatic) and asymmetric (non-adiabatic) state transfer regimes for the same set of initial eigenmodes by appropriately varying the system parameters. In other words, we realize a fully programmable symmetric-asymmetric two-mode switch which has been thought impossible to implement in such two-level systems. This is in striking contrast to previous studies[50], where the realization of a programmable state switch requires high-dimensional multimode systems and relies on the nontrivial interplay between exceptional and diabolic points in the Hamiltonian spectrum.

These results open new avenues for non-Hermitian state-control protocols in both classical and quantum photonic platforms, with potential implications for topological quantum computation[51–55] and related areas of classical and quantum information processing. In particular, the symmetric state-switching protocol demonstrated here in a minimal two-level photonic building block can, in principle, be scaled to implement controlled topological state permutations in multi-qubit systems[44]; for example, in integrated photonic architectures or networks of coupled waveguides and/or cavities, where it could realize SWAP-type quantum gate operations[56]. The controlled implementation of symmetric group operations in the non-Hermitian qubit eigenspace may enable topological quantum-computation schemes, where resulting holonomies generated by encircling EPs can be exploited as robust logical operations[52,57,58].

Methods

Eigenvectors of the NHH H

The eigenvectors of the NHH H in Eq. (4) can be readily derived as

$$|\psi_1\rangle = \left[-\sin\frac{\phi}{2}, \cos\frac{\phi}{2}\right]^T, |\psi_2\rangle = \left[\cos\frac{\phi}{2}, \sin\frac{\phi}{2}\right]^T, \tag{11}$$

and the corresponding left eigenvectors

$$|\eta_1\rangle = \left[-\sin\frac{\phi^*}{2}, \cos\frac{\phi^*}{2}\right]^T, |\eta_2\rangle = \left[\cos\frac{\phi^*}{2}, \sin\frac{\phi^*}{2}\right]^T, \tag{12}$$

where T stands for transpose, and the right eigenvectors and corresponding left eigenvectors form the biorthogonal basis[59,60], namely, $\langle\eta_j|\psi_k\rangle = \delta_{jk}$.

The right eigenvectors satisfy $H|\psi_k\rangle = E_k|\psi_k\rangle$, and the corresponding left eigenvectors $|\eta_j\rangle$ are defined via the equation $H^\dagger|\eta_j\rangle = E_j^*|\eta_j\rangle$. The set of left and right eigenvectors forms the biorthonormal basis

$$\langle\eta_j|\psi_k\rangle = \delta_{jk}, \tag{13}$$

along with the closure relation

$$\sum_j |\psi_j\rangle\langle\eta_j| = I. \tag{14}$$

It is important to note that the right eigenstates alone are, in general, non-orthogonal. The introduction of the left eigenstates, which span the dual vector space, is therefore essential. The non-orthogonality of right eigenvectors can be interpreted as a manifestation of the “non-flatness” in the NHH-Hilbert space. Such a curved space must be endowed with a metric tensor ν, where the left eigenvectors enable us to define a consistent tensor $\nu = \sum|\eta_m\rangle\langle\eta_m|$. The metric ν is essential for properly defining inner products between arbitrary (right) vectors in this non-flat space, $|\psi_{m,n}\rangle$ as $\langle\psi_m|\psi_n\rangle_{\text{flat}} \to \langle\psi_m|\nu|\psi_n\rangle_{\text{nonflat}}$, ensuring norm preservation and probabilistic interpretation throughout the time evolution[42,61,62].

Experimental implementation: state preparation, evolution, and measurement procedure

In our experiment, as mentioned above, we simulate the continuous system dynamics by appropriately constructing the corresponding operator $U(t)$, which effectively mimics the induced time evolution. This is achieved as follows. At the beginning, by restricting the system parameters to the 2D manifold within the full 4D parameter space, one reduces the NHH $H_0(t) \to H(t)$, which generally exhibits complex eigenvalues, into a parameter regime where the spectrum becomes purely real. For a given point on the trajectory, the Hamiltonian parameters $\{\upsilon(t), \epsilon(t), \kappa(t), u(t)\}$ are determined by $\{x(t), y(t)\}$. After that, we compute the target cumulative evolution operator $U(t)$, according to Eq. (8), and decompose this target operator into the form $U(t) = R_1LR_2$ via the singular value decomposition.

In practice, these four parameters $\{\upsilon(t), \epsilon(t), \kappa(t), u(t)\}$ collectively contribute to each element of the matrix $U(t)$. However, for coherence parameters (detuning ϵ, coherent coupling u), the unitary parts of the evolution, which mix the polarization modes (basis rotations), are mainly encoded in the rotation matrices R_1 and R_2. These are implemented by adjusting the waveplate angles in the two variable polarization controllers. For non-Hermitian parameters (gain/loss υ, dissipative coupling κ), the non-unitary feature is primarily encoded in the diagonal matrix L. This is physically implemented by controlling the gain/loss ratio between the two split optical paths using the variable optical attenuator and erbium-doped fiber amplifiers together with the optical delay line.

As illustrated in Fig. 1b, our experimental platform consists of three main stages: the state preparation, the evolution, and the measurement.

In our work, the initial states we select are two right eigenstates in Eq. (11). After normalizing each of them, we encode the two orthogonal components of each state onto the horizontal and vertical polarizations of the polarized light, which matches well with the Jones vector[63,64]. This is conducive to a better experimental implementation. Experimentally, the initial eigenstate can be encoded in the polarization state of the light pulse $\vec{J} = [a_0, b_0]^T = |\psi_k(t=0)\rangle$ $(k = 1, 2)$, where the state $|\psi_k\rangle$ is normalized. Here, the horizontal and vertical components of a light pulse are represented by a_0 and b_0, respectively. As illustrated in Fig. 1b, a 266.7 ns laser pulse at a wavelength of 1550 nm (generated by a distributed feedback laser diode and an acousto-optic modulator) featuring an original state of polarization goes through the variable polarization controller. The variable polarization controller can realize the required 2 × 2 unitary transformation. This is because it is equivalent to a sandwiched combination of two quarter-wave plates and one half-wave plate (Q–H–Q) by controlling the phase delay amount[47,65,66]. The Jones matrix form for a half-wave plate at the setting angle φ is[37]

$$U_h = \begin{pmatrix} \cos(2\varphi) & \sin(2\varphi) \\ \sin(2\varphi) & -\cos(2\varphi) \end{pmatrix}, \tag{15}$$

and the Jones matrix form for a quarter-wave plate at the setting angle ς is

$$U_q = \begin{pmatrix} \cos^2\varsigma + i\sin^2\varsigma & (1-i)\sin\varsigma\cos\varsigma \\ (1-i)\sin\varsigma\cos\varsigma & \sin^2\varsigma + i\cos^2\varsigma \end{pmatrix}. \tag{16}$$

Therefore, by controlling the rotation angle of the tunable polarization controller, we can prepare the desired initial state[47]. After measurement with a polarimeter, we can verify the quality of the state preparation. The polarimeter we use can obtain the normalized power split ratio and the phase difference of the horizontal and vertical polarization components, which can determine the form of the polarization state. We calculate the fidelity between the experimentally prepared initial states and the theoretically designed initial states as: $99.92\% \pm 0.04\%$ for $|\psi_1\rangle$ and $99.72\% \pm 0.05\%$ for $|\psi_2\rangle$, indicating that the prepared initial states are highly consistent with the theory. Then the pulse with the prepared initial state is injected into the main optical path, and subsequent operations are carried out.

After the initial state preparation, by employing two such variable polarization controllers, we realize the unitary matrices R_1 and R_2. A polarization beam splitter then separates the horizontal and vertical polarization components of a light beam into two independent modes. Each mode undergoes a distinct gain or loss modulation, enabling the realization of a real diagonal matrix L, where l_1 and l_2 are respectively regarded as the gain and loss coefficients related to an erbium-doped fiber amplifier and the variable optical attenuator, and appropriately scaling both modes simultaneously by the same global gain or loss factor does not alter the normalized evolving state. Additionally, if needed, phase modulation can also be applied to each mode via phase modulators. Here, the optical delay line is also deployed to balance the length of the two modes. Then, the two modes are subsequently recombined using a polarization beam combiner. To compensate for the insertion losses introduced by electro-optical and fiber components, an additional erbium-doped fiber amplifier is inserted into the two-mode rail optical system to prevent pulse attenuation.

At the end of the evolution path, half of the optical pulses are directed to a polarimeter for polarization state analysis. The remaining pulses are used for monitoring purposes via an oscilloscope. In the experiment, we select the discrete time points $(\omega t)_m = (m\Delta N - \frac{1}{2}) \times \frac{2\pi}{N}$ with $\Delta N = N/20$, $m = 1, \ldots, 20$, $\delta_t = t/N$, $\omega = \pi/50000$ and $N = 5 \times 10^4$, as shown in Fig. 2. Here, N refers to the number of steps in the numerical integration (the total number of segments as mentioned above) used in the theoretical calculation of the target operator $U(t)$. We use a large N to ensure the theoretical matrix is computed with high precision, rather than feed the signal back 5×10^4 times in the experiment. Then, we experimentally measure the polarization state of the system, projected onto the instantaneous left eigenstates, and thereby obtain the relative eigenstate population $P(t)$. The deviations are dominated by experimental imperfections in implementing the non-unitary evolution operator and measurement uncertainties, which include contributions from instrument instability, environmental fluctuations, and disturbances introduced by the optical fibers.

Data availability

The data that support the findings of this study are available via Zenodo at https://doi.org/10.5281/zenodo.19604811.

Code availability

The code that supports the findings of this study is available via Zenodo at https://doi.org/10.5281/zenodo.19604811.

References

1. El-Ganainy, R. et al. Non-Hermitian physics and PT symmetry. *Nat. Phys.* **14**, 11 (2018).
2. Müller, M. & Rotter, I. Exceptional points in open quantum systems. *J. Phys. A* **41**, 244018 (2008).
3. Miri, M.-A. & Alù, A. Exceptional points in optics and photonics. *Science* **363**, eaar7709 (2019).
4. Insinga, A., Andresen, B., Salamon, P. & Kosloff, R. Quantum heat engines: limit cycles and exceptional points. *Phys. Rev. E* **97**, 062153 (2018).
5. Lin, Z. et al. Unidirectional invisibility induced by PT-symmetric periodic structures. *Phys. Rev. Lett.* **106**, 213901 (2011).
6. Feng, L. et al. Experimental demonstration of a unidirectional reflectionless parity-time metamaterial at optical frequencies. *Nat. Mater.* **12**, 108 (2013).
7. Peng, B. et al. Chiral modes and directional lasing at exceptional points. *Proc. Natl. Acad. Sci. USA*. **113**, 6845–6850 (2016).
8. Liu, Z. et al. Metrology with PT-symmetric cavities: enhanced sensitivity near the PT-phase transition. *Phys. Rev. Lett.* **117**, 110802 (2016).
9. Hodaei, H., Miri, M., Heinrich, M., Christodoulides, D. N. & Khajavikhan, M. Parity-time-symmetric microring lasers. *Science* **346**, 975 (2014).
10. Peng, B. et al. Loss-induced suppression and revival of lasing. *Science* **346**, 328 (2014).
11. Schumer, A. et al. Topological modes in a laser cavity through exceptional state transfer. *Science* **375**, 884–888 (2022).
12. Hodaei, H. et al. Enhanced sensitivity at higher-order exceptional points. *Nature (London)* **548**, 187 (2017).
13. Chen, W., Kaya Özdemir, Ş, Zhao, G., Wiersig, J. & Yang, L. Exceptional points enhance sensing in an optical microcavity. *Nature* **548**, 192–196 (2017).
14. Zhang, M. et al. Quantum noise theory of exceptional point amplifying sensors. *Phys. Rev. Lett.* **123**, 180501 (2019).
15. Wu, Q.-C. et al. Shortcuts to adiabatic state transfer in time-modulated two-level non-Hermitian systems. *Phys. Rev. A* **111**, 022410 (2025).
16. Song, P. et al. Experimental realization of on-chip few-photon control around exceptional points. *Nat. Commun.* **15**, 9848 (2024).
17. Özdemir, ŞK., Rotter, S., Nori, F. & Yang, L. Parity-time symmetry and exceptional points in photonics. *Nat. Mater.* **18**, 783 (2019).
18. Ashida, Y., Gong, Z. & Ueda, M. Non-Hermitian physics. *Adv. Phys.* **69**, 249–435 (2020).
19. Heiss, W. D. Repulsion of resonance states and exceptional points. *Phys. Rev. E* **61**, 929–932 (2000).
20. Cartarius, H., Main, J. & Wunner, G. Exceptional points in atomic spectra. *Phys. Rev. Lett.* **99**, 173003 (2007).
21. Dembowski, C. et al. Experimental observation of the topological structure of exceptional points. *Phys. Rev. Lett.* **86**, 787–790 (2001).
22. Dietz, B. et al. Exceptional points in a microwave billiard with time-reversal invariance violation. *Phys. Rev. Lett.* **106**, 150403 (2011).
23. Gao, T. et al. Observation of non-Hermitian degeneracies in a chaotic exciton-polariton billiard. *Nature (London)* **526**, 554–558 (2015).
24. Ding, K., Ma, G., Xiao, M., Zhang, Z. Q. & Chan, C. T. Emergence, coalescence, and topological properties of multiple exceptional points and their experimental realization. *Phys. Rev. X* **6**, 021007 (2016).
25. Ergoktas, M. S. et al. Topological engineering of terahertz light using electrically tunable exceptional point singularities. *Science* **376**, 184–188 (2022).
26. Guria, C. et al. Resolving the topology of encircling multiple exceptional points. *Nat. Commun.* **15**, 1369 (2024).
27. Doppler, J. et al. Dynamically encircling an exceptional point for asymmetric mode switching. *Nature (London)* **537**, 76 (2016).
28. Hassan, A. U., Zhen, B., Soljačić, M., Khajavikhan, M. & Christodoulides, D. N. Dynamically encircling exceptional points: exact evolution and polarization state conversion. *Phys. Rev. Lett.* **118**, 093002 (2017).

29. Xu, H., Mason, D., Jiang, L. & Harris, J. G. E. Topological energy transfer in an optomechanical system with exceptional points. *Nature (London)* **537**, 80–83 (2016).
30. Yoon, J. W. et al. Time-asymmetric loop around an exceptional point over the full optical communications band. *Nature (London)* **562**, 86 (2018).
31. Zhang, X.-L., Wang, S., Hou, B. & Chan, C. T. Dynamically encircling exceptional points: in situ control of encircling loops and the role of the starting point. *Phys. Rev. X* **8**, 021066 (2018).
32. Zhang, X.-L., Jiang, T. & Chan, C. T. Dynamically encircling an exceptional point in anti-parity-time symmetric systems: asymmetric mode switching for symmetry-broken modes. *Light Sci. Appl.* **8**, 88 (2019).
33. Feilhauer, J. et al. Encircling exceptional points as a non-Hermitian extension of rapid adiabatic passage. *Phys. Rev. A* **102**, 040201 (2020).
34. Liu, W., Wu, Y., Duan, C., Rong, X. & Du, J. F. Dynamically encircling an exceptional point in a real quantum system. *Phys. Rev. Lett.* **126**, 170506 (2021).
35. Feng, Z. & Sun, X. Harnessing dynamical encircling of an exceptional point in anti-$\mathcal{PT}$-symmetric integrated photonic systems. *Phys. Rev. Lett.* **129**, 273601 (2022).
36. Tang, Z., Chen, T. & Zhang, X. Highly efficient transfer of quantum state and robust generation of entanglement state around exceptional lines. *Laser Photonics Rev.* **18**, 2300794 (2023).
37. Gao, H. et al. Photonic chiral state transfer near the Liouvillian exceptional point. *Phys. Rev. Lett.* **134**, 146602 (2025).
38. Uzdin, R., Mailybaev, A. & Moiseyev, N. On the observability and asymmetry of adiabatic state flips generated by exceptional points. *J. Phys. A* **44**, 435302 (2011).
39. Berry, M. V. Optical polarization evolution near a non-Hermitian degeneracy. *J. Opt. A* **13**, 115701 (2011).
40. Graefe, E.-M., Mailybaev, A. A. & Moiseyev, N. Breakdown of adiabatic transfer of light in waveguides in the presence of absorption. *Phys. Rev. A* **88**, 033842 (2013).
41. Chen, W. et al. Decoherence-induced exceptional points in a dissipative superconducting qubit. *Phys. Rev. Lett.* **128**, 110402 (2022).
42. Arkhipov, I. I., Minganti, F., Miranowicz, A., Özdemir, S. K. & Nori, F. Restoring adiabatic state transfer in time-modulated non-Hermitian systems. *Phys. Rev. Lett.* **133**, 113802 (2024).
43. Leefmans, C. et al. Topological dissipation in a time-multiplexed photonic resonator network. *Nat. Phys.* **18**, 442 (2022).
44. Arkhipov, I. I., Lewalle, P., Nori, F., Özdemir, I. M. C. K. & Whaley, K. B. Topological state permutations in time-modulated non-Hermitian multiqubit systems with suppressed nonadiabatic transitions. *Phys. Rev. Res.* **7**, 033242 (2025).
45. Metcalf, H. Colloquium: Strong optical forces on atoms in multifrequency light. *Rev. Mod. Phys.* **89**, 041001 (2017).
46. Xiao, L. et al. Observation of critical phenomena in parity-time-symmetric quantum dynamics. *Phys. Rev. Lett.* **123**, 230401 (2019).
47. Nasari, H. et al. Observation of chiral state transfer without encircling an exceptional point. *Nature* **605**, 256–261 (2022).
48. Scheel, S. & Szameit, A. $\mathcal{PT}$ -symmetric photonic quantum systems with gain and loss do not exist. *Europhys. Lett.* **122**, 34001 (2018).
49. Klauck, F. et al. Observation of parity-time symmetry in quantum interference. *Nat. Photon.* **13**, 883 (2019).
50. Arkhipov, I. I., Miranowicz, A., Minganti, F., Özdemir, ŞK. & Nori, F. Dynamically crossing diabolic points while encircling exceptional curves: a programmable symmetric-asymmetric multimode switch. *Nat. Commun.* **14**, 2076 (2023).
51. Chen, Y. H., Qin, W., Stassi, R., Wang, X. & Nori, F. Fast binomial-code holonomic quantum computation with ultrastrong light-matter coupling. *Phys. Rev. Res.* **3**, 033275 (2021).
52. Zhang, J. et al. Geometric and holonomic quantum computation. *Phys. Rep.* **1027**, 1 (2023).
53. Qin, W., Wang, C., Cao, Y. & Long, G. L. Multiphoton quantum communication in quantum networks. *Phys. Rev. A* **89**, 062314 (2014).
54. Cheng, X. et al. A chip-scale polarization-spatial-momentum quantum swap gate in silicon nanophotonics. *Nat. Photonics* **17**, 656–665 (2023).
55. Zhang, J., Devitt, S. J., You, J. Q. & Nori, F. Holonomic surface codes for fault-tolerant quantum computation. *Phys. Rev. A* **97**, 022335 (2018).
56. Cheng, X. et al. A chip-scale polarization-spatial-momentum quantum SWAP gate in silicon nanophotonics. *Nat. Photon.* **17**, 656–665 (2023).
57. Zanardi, P. & Rasetti, M. Holonomic quantum computation. *Phys. Lett. A* **264**, 94–99 (1999).
58. Duan, L.-M., Cirac, J. I. & Zoller, P. Geometric manipulation of trapped ions for quantum computation. *Science* **292**, 1695–1697 (2001).
59. Brody, D. C. Biorthogonal quantum mechanics. *J. Phys. A* **47**, 035305 (2014).
60. Wu, Q. C. et al. Extension of Noether's theorem in PT-symmetry systems and its experimental demonstration in an optical setup. *Sci. China Phys. Mech. Astron.* **66**, 240312 (2023).
61. Ju, C.-Y., Miranowicz, A., Chen, G.-Y. & Nori, F. Non-Hermitian Hamiltonians and no-go theorems in quantum information. *Phys. Rev. A* **100**, 062118 (2019).
62. Mostafazadeh, A. Pseudo-Hermitian representation of quantum mechanics. *Int. J. Geom. Methods Mod. Phys.* **07**, 1191 (2010).
63. Jones, R. C. A new calculus for the treatment of optical systems I. Description and discussion of the calculus. *J. Opt. Soc. Am.* **31**, 488–493 (1941).
64. Hecht, E. Optics. Addison Wesley: New York, 2016.
65. Ulrich, R. & Simon, A. Polarization optics of twisted single-mode fibers. *Appl. Opt.* **18**, 2241–2251 (1979).
66. Moroney, N. et al. A Kerr polarization controller. *Nat. Commun.* **13**, 398 (2022).

Acknowledgements

This work has been supported by the National Key R&D Program of China (Grant No. 2023YFA1406701) and the National Natural Science Foundation of China (Grant Nos. 92265209, 92476106, 12504587, 12305008, 12374479, 12504413, 12025401). I.A. acknowledges support from the Grant Agency of the Czech Republic (Project No. 25-15775S), and from the Ministry of Education, Youth and Sports of the Czech Republic, Grant OP JAC No. CZ.02.01.01/00/23_021/0008790. F.N. is supported in part by the Japan Science and Technology Agency (JST) [via the CREST Quantum Frontiers program Grant No. JPMJCR24I2, the Quantum Leap Flagship Program (Q-LEAP), and the Moonshot R&D Grant Number JPMJMS2061]. Q.L. acknowledges support from the China Postdoctoral Science Foundation (Grant No. BX20240065 and No. 2024M750405) and the Basic Research Program of Jiangsu (Grants No. BK20251297). H.X.G. acknowledges support from the China Postdoctoral Science Foundation (Grant No. BX20250174 and No. 2024M760425). D.K.Q. acknowledges support from the China Postdoctoral Science Foundation (Grants No. BX20230036 and No. 2023M730198). L.X. acknowledges support from Beijing National Laboratory for Condensed Matter Physics (No. 2024BNLCMPKF010).

Author contributions

X.W.W. performed the experiment and interpreted the results with contributions from Q.L., H.X.G., D.K.Q., and L.X. I.I.A. developed the theoretical aspects and interpreted the results with contributions from F.N. P.X. supervised the project, and analyzed the results. All authors contributed to writing the paper.

Competing interests

The authors declare no competing interests.

Additional information

Supplementary information The online version contains supplementary material available at https://doi.org/10.1038/s41467-026-72751-8.

Correspondence and requests for materials should be addressed to Peng Xue.

Peer review information *Nature Communications* thanks Kater Murch and the other, anonymous, reviewers for their contribution to the peer review of this work. A peer review file is available.

Reprints and permissions information is available at http://www.nature.com/reprints